Design of Two-Phase Injectors Using Analytical and Numerical Methods with Application to Hybrid Rockets

Emerson Vargas Niño[*] and Mohammad Reza Razavi[†]
University of Toronto, Toronto, Ontario, M3H 5T6, Canada

Liquid injectors under certain conditions may experience cavitation, resulting in two-phase flow which complicates their design and analysis as traditional mass flow rate models are invalid. We evaluated a wide range of analytical models from the literature and concluded that they fall short of a definitive prediction of two-phase mass flow rate.

We addressed this problem by proposing a model capable of predicting mass flow rate and critical pressure with an average error of 3.9%. CFD simulation results using different numerical approaches are presented. An Euler-Euler-VOF hybrid solver predicts mass flow rate with an average error of 3.6%. A design methodology incorporating the analytical and CFD models is presented and used to design a two-phase axial injector for a N_2O-Paraffin hybrid rocket engine.

I. Nomenclature

D	=	Injector diameter
G	=	Mass flux
h	=	Specific enthalpy
L	=	Injector length
$\dot{m}$	=	Mass flow rate
P	=	Pressure
T	=	Temperature
t	=	Time
U	=	Velocity
α	=	Liquid volume fraction
η	=	Pressure ratio with respect to inlet pressure
ν	=	Specific volume
ρ	=	Density
χ	=	Vapor mass quality
ω	=	Omega parameter
$()_{cc}$	=	Combustion chamber
$()_{ox}$	=	Oxidizer tank
$()_i$	=	Injector inlet
$()_o$	=	Injector outlet
$()_{crit}$	=	Critical choking point
$()_{low}$	=	Low supercharged state
$()_{high}$	=	High supercharged state
$()_{super}$	=	Supercharged state
$()_{sat}$	=	Saturated state
$()_k$	=	Liquid, gas phase index
$()_l$	=	Liquid conditions
$()_g$	=	Gas conditions
$()_{lg}$	=	Difference between liquid and gas phase properties

---

[*]Graduate Student, Institute for Aerospace Studies, Student Member AIAA.
[†]Undergraduate Student, Division of Engineering Science, Student Member AIAA.

II. Introduction

Reliable hybrid rocket performance is dependent on many factors. Injector design is critical in both the performance and stability of the engine. A well designed injector can lead to a decrease of combustion instabilities and can lead to improved combustion efficiency [1, 2].

Nitrous Oxide (N_2O) is a common oxidizer used in hybrid rockets which is favorable due to its high saturation pressure at room temperature and low handling and storage requirements. However, designing an injector for a fluid at its saturation pressure presents complications. When a fluid accelerates through a constrained volume its pressure drops due to the accelerating flow. If the pressure drops below its saturation pressure for the given temperature, the fluid will experience a phase change process termed cavitation.

The University of Toronto Aerospace Team (UTAT) is currently developing *Defiance*, a N_2O-Paraffin hybrid rocket designed to break the Canadian amateur rocketry altitude record. The engine, *Quasar*, has a design thrust of 6700 N and will power the rocket to an altitude over 18 km. The N_2O oxidizer is operating at saturation conditions. Thus the saturation pressure of the N_2O alone is used to pressurize the oxidizer, eliminating the need for a heavy pressurizing system and leading to significant mass reductions.

The present study aims to provide a design methodology for cavitating N_2O injector elements for use in a hybrid rocket engine. The paper is divided into the following sections: The origins and applications of cavitation are discussed. An overview of analytical models is provided and a selected set are implemented. The internal flow structure is studied through a range of CFD methodologies. Lastly, a simplified process is conceived to optimize the design of axial N_2O injectors for use in hybrid rockets and the process is applied to UTAT's N_2O-Paraffin *Quasar* engine.

III. Background

### A. Cavitation and Choking in Hybrid Rockets

A saturated fluid, at its saturation pressure, forced through a constrained volume will experience a drop in pressure and an increase in velocity. As the saturation pressure marks the liquid-gas transition point, the drop in pressure will force the liquid to become a two-phase mixture. A supercharged fluid (also referred to as a subcooled fluid, a state in which the pressure is higher than the fluid's saturation pressure at the given temperature) can also enter the two-phase region, given a sufficiently large pressure drop. This phenomenon often manifests itself in the form of bubble formation within the flow and is termed cavitation. The fluid across the volume will continue to experience an increase in velocity and mass flow rate as the pressure further drops until the fluid velocity reaches the local sonic velocity. At this point, the flow is said to be choked, the mass flow rate stops increasing and is termed "critical mass flow rate". Downstream pressure changes are unable to interfere with upstream conditions as pressure waves are unable to travel upstream due to the sonic conditions.

The inception of cavitation depends on many factors such as the thermodynamic path of the pressure drop, the total stress experienced by the fluid and the availability of nucleation sites [3]. In some cases cavitation might not occur (even if the pressure drops below the saturation pressure) if the liquid enters the metastable phase [4].

In practice, cavitation may present a range of problems depending on the application. Following a cavitating region the local pressure may increase leading to the collapse of cavitation bubbles resulting in instantaneous jets with pressure shocks as high as 689.5 MPa. This can cause pitting in the surfaces involved leading to damaged equipment, excessive noise and vibration [5].

Modeling the factors that influence choking and accounting for the two-phase transition path, is the subject of a large body of research in the nuclear industry for high pressure water line breaks, automotive industry for diesel fuel injectors in engines, gas industry for cracks in CO_2 pipelines, cooling systems incorporating certain refrigerants, and in safety pressure relief valves for fluid storage. In all these applications, the presence of fluids at saturated or supercharged conditions coupled with a crack or small orifice causes cavitating, two-phase, critical choked flow. Thus, the modelling of this flow is paramount to be able to control the fluids utilized.

Cavitating, choked flow in N_2O injectors presents many great benefits for hybrid rocket engine performance. The constant mass flow rate allows the engine thrust to remain at the nominal design point throughout the burn. Feed system coupled instabilities, typical in hybrid rockets, can be reduced or eliminated due to the choked flow. In addition, the collapse of cavitation bubbles inside an injector leads to increased levels of turbulence at the exit plane which serve to enhance atomization [6] leading to increased stability and efficiency of the combustion process [2].

2
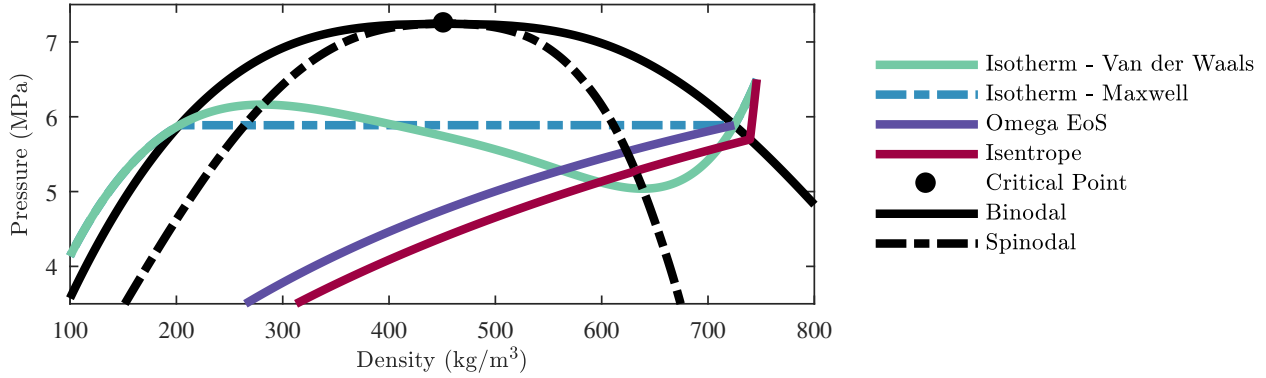
Fig. 1   Possible thermodynamic decompression paths for supercharged N$_2$O injection from an initial pressure of 6.5 MPa and a temperature of 300 K.

Table 1   Classification of common analytical two-phase mass flow models.

Classification	Models
Homogeneous Equilibrium	HEM [1], Omega [7, 8]
Non-Homogeneous Equilibrium	Moody [1, 9], Fauske [1], Modified Henry-Fauske [9]
Homogeneous Non-Equilibrium	HRM [10], DEM [11]
Non-Homogeneous Non-Equilibrium	Dyer [12]

B. Thermodynamic Decompression Paths

At the onset of cavitation, as the fluid enters the two-phase region below the binodal, as seen in Fig. 1, the depressurization path is bounded by a Maxwellian isotherm and an isentrope, corresponding to an infinitely slow isothermic process and an infinitely fast isentropic process respectively [1]. In practice, the exact thermodynamic path the fluid takes through the two-phase region is difficult to predict and is a major source of difficulty when modeling two-phase flows. Figure 1 presents different thermodynamic paths for a typical depressurization case for initially supercharged N$_2$O calculated using equations of state implemented in the REFPROP [13] and CoolProp [14] thermodynamic libraries.

C. Metastable Phase

Due to a finite rate of heat transfer and the availability of nucleation sites, it has been shown that a fluid at the onset of cavitation may enter a metastable phase where it remains a liquid below its saturation pressure. This process is sometimes referred to as pressure undershoot. The theoretical limit of the metastable phase is the spinodal line, which can be determined based on the Van der Waals equation of state (EoS). It has been shown through numerous experiments that the possible extent of metastability is given by 95% of the saturation pressure [11]. This can present a method for predicting the onset of nucleation in the flow, and has been accounted for in some two-phase analytical models such as the DEM and modified Henry-Fauske models [9, 11].

D. Similarities between N$_2$O and CO$_2$

Although N$_2$O is the primary fluid in this study, CO$_2$ is recognized as a suitable alternative for non-combusting fluid flow studies as the two fluids have similar molecular and thermodynamic properties [1]. Additionally, unlike N$_2$O, CO$_2$ does not have the risk of potentially undergoing a violent and rapid exothermic decomposition, and is thus inherently safer [1].

IV. Mass Flow Rate Models

There are several approaches to predict two-phase mass flow, including empirical relations, analytical models, and CFD simulations. Empirical models can be used provided the experiments they are based on are sufficiently relevant. Analytical models are more general in their application and can be divided into four classes, depending on homogeneity

and equilibrium assumptions, where homogeneity refers to the assumption of slip between the phases and equilibrium refers to the assumption of temperature change in the depressurization process. Table 1 lists different analytical models of differing popularity and their classification. A subset of these models are implemented to model the mass flow rate through the injector elements and are described as follows.

A. Single Phase Incompressible

The Bernoulli derived single phase incompressible (SPI) model assumes a steady, single phase, incompressible, inviscid liquid undergoing an isentropic depressurization. The corresponding mass flux is given by,

$$G = C_\mathrm{d}\sqrt{2\rho_l(P_\mathrm{i} - P_\mathrm{o})} \tag{1}$$

The choice of discharge coefficient C_d is discussed in section IV.I. This model is the simplest and most widely used for high-level injector design. It tends to overpredict the flow rate for high pressure drops.

B. Homogeneous Equilibrium Model

The homogeneous equilibrium model (HEM) model uses changes in enthalpy during an isentropic depressurization to predict the mass flux of a two-phase fluid. The upstream enthalpy is known (from the upstream state), and the downstream enthalpy can be calculated following a line of constant entropy through the EoS implemented in REFPROP [13] or CoolProp [14]. The mass flux is given by,

$$G = C_\mathrm{d}\rho_\mathrm{o}\sqrt{2(h_\mathrm{i} - h_\mathrm{o})} \tag{2}$$

The traditional HEM model predicts an increasing mass flux with increasing pressure drop until a critical pressure where the mass flux begins to drop. To prevent modeling this unphysical behavior, we hold the maximum mass flux constant past the critical pressure drop to model the choking behavior.

C. Non-Homogeneous Non-Equilibrium Model

Dyer et. al. [12] proposed that finite vapor growth rates within small cavitating injector elements are a major source of non-equilibrium effects and attempted to model this through the use of a non-equilibrium parameter κ, proportional to the ratio of bubble growth time τ_b and fluid residence time τ_r. The parameter is used to represent the amount of vapor that can form within an injector element given a finite residence time. The model predicts a mass flux bounded by the SPI and HEM models. The resulting non-homogeneous non-equilibrium (NHNE) model has been widely applied to hybrid rockets with varying degrees of success [1, 15]. The resulting mass flux is given by,

$$G = \left(1 - \frac{1}{1 + \kappa}\right)G_\mathrm{SPI} + \left(\frac{1}{1 + \kappa}\right)G_\mathrm{HEM} \tag{3}$$

where κ can be simplified from a relation of time scales to one of upstream and downstream pressures given by,

$$\kappa = \sqrt{\frac{P_\mathrm{i} - P_\mathrm{o}}{P_\mathrm{sat} - P_\mathrm{o}}} \tag{4}$$

At saturated conditions the NHNE model loses its physical interpretation as the value of κ is unity and the resulting mass flux given by Eq. (3) is simply an equal averaging of the SPI and HEM models.

D. Modified Henry-Fauske

S. Yin et. al. [9] applied the theories of rapid depressurization and isothermal bubble growth to the well known Moody and Henry-Fauske mass flow models. The modifications allow the nucleation inception point to account for the effect of channel geometry and decompression through the metastable phase leading to improved model accuracy.

This model can only predict the choked mass flow rate and the critical pressure at which it occurs. Hence it is applicable for all pressure drops higher than the chocking pressure. Such models will be termed critical models. For chamber pressures below the choking pressure, the Dyer model is used and connected to the choked mass flow rate at the critical pressure drop point through a blending function. The model's critical mass flux is given by,

$$G_\mathrm{crit} = \left\{ \frac{d}{dp_\mathrm{crit}} \left[\frac{|U|(\nu_l S - \chi\nu_l S + \chi\nu_g)(\chi S - \chi + 1)}{\nu S} \right] \right\}^{-1} \tag{5}$$

4

E. X. Fan et. al. Model

X. Fan et. al. [16] conducted experiments with supercritical CO_2 in 1 mm diameter axial injectors with length to diameter ratios between 1 and 15. An empirical correlation accounting for geometric and thermal effects was subsequently developed based on the experimental results. Although the test conditions were supercritical and therefore different than the case at hand, the empirical correlation was applied regardless due to its simplicity, yielding acceptable results.

Similarly to the Modified Henry-Fauske model in section IV.D, this model is a critical model. As such it is also connected to the Dyer model through a blending function. The predicted critical mass flux is given by Eq. (6) where the subscript ( )$_{\text{critical}}$ describes the thermodynamic critical point.

$$G_{\text{crit}} = \left(0.5463 + 0.0587\left(\frac{P_i}{P_{\text{critical}}}\right)^{2.07}\left(\frac{\rho_i}{\rho_{\text{critical}}}\right)^{-0.939}\right)\sqrt{2\rho_i(P_i - P_o)} \tag{6}$$

F. Omega model

The Omega model proposes an EoS for the thermodynamic decompression path given by,

$$\frac{\rho_i}{\rho} = \omega\left(\frac{P_i}{P} - 1\right) + 1 \tag{7}$$

The defining feature of the Omega model is the ω parameter given in Eq. (8), which is only a function of upstream properties. Here $c_{l,i}$ is the specific heat capacity of the liquid phase at the inlet.

$$\omega = \frac{\chi_i v_{lg,i}}{v_i} + \frac{c_{l,i}T_iP_i}{v_i}\left(\frac{v_{lg,i}}{h_{lg,i}}\right)^2 \tag{8}$$

The Omega model's EoS, shown in Fig. 1, follows a path similar to isentropic expansion. The offset between the paths is because the Omega model's EoS assumes that the initial pressure is the saturation pressure corresponding to the initial temperature, even for supercharged inlet conditions. Therefore, the depressurization into the two-phase regime begins at the same point as the isothermal line.

The Omega model uses different equations to predict mass flow rate based on saturated, low supercharging, or high supercharging inlet conditions. The details of the derivation are omitted and are available in [7] and [8].

For the saturated case, the critical mass flux is given by,

$$G_{\text{sat,crit}} = \sqrt{P_i\rho_{l,i}}\frac{\eta_{\text{crit}}}{\sqrt{\omega}} \tag{9}$$

For supercharged fluids, the division between low and high supercharging is determined using the η_{st} parameter given by Eq. (10), where ω is evaluated at saturated conditions,

$$\eta_{\text{st}} = \frac{2\omega_{sat}}{1 + 2\omega_{sat}} \tag{10}$$

For the data used η_{st} evaluates to approximately 0.75. To determine if the inlet pressure is in a low or high supercharged state, denoted by the subscript low and high respectively, it is scaled by η_{st} to give a reduced inlet pressure and compared with the saturation pressure.

In a high supercharged state, the saturation pressure is less than the reduced inlet pressure ($P_{\text{sat}} < \eta_{\text{st}}P_i$). The predicted critical pressure is the saturation pressure, and the choked mass flux $G_{\text{high,crit}}$ is given by,

$$G_{\text{high,crit}} = \rho_i\sqrt{2P_i(P_i - P_{\text{sat}})} \tag{11}$$

In a low supercharged state the saturation pressure is greater than the reduced inlet pressure ($P_{\text{sat}} > \eta_{\text{st}}P_i$). The choking pressure is calculated implicitly [7], and the mass flux is given by,

$$\frac{G_{\text{low}}}{\sqrt{P_i/v_{l,i}}} = \frac{\sqrt{2(1-\eta_{\text{sat}}) + 2[\omega_{\text{sat}}\eta_{\text{sat}}\ln(\eta_{\text{sat}}/\eta) - (\omega_{\text{sat}}-1)(\eta_{\text{sat}}-\eta)]}}{\omega_{\text{sat}}(\eta_{\text{sat}}/\eta - 1) + 1} \tag{12}$$

G. Modified Omega Model

Since the Omega model is derived for ideal nozzles, it presents discrepancies when applied to real nozzles. Typically this is addressed by experimentally derived discharge coefficients, however they may not be available in the design phase. We propose modifications to the Omega model to address these discrepancies for general applications. Frictional losses are due to the presence of injector walls, which are ignored in the ideal nozzle assumption. When the flow is choked, the geometry of the real nozzle after the choke point does not play a role in the flow rate as there is no upstream propagation. This reduces the effective real geometric surface area and the real nozzle is closer to the ideal nozzle assumption. This means the error in the Omega model is lower for cases where the flow is choked. For cases where the flow is not choked and the effects of geometry do play a significant role in the mass flow rate, the error in the model is large [17].

Flow through straight port, sharp edge nozzles increases the total stress of the fluid and contributes to cavitation [3]. Combined with the formation of gas pockets by the vena contracta, flow through this type of nozzle is much more prone to cavitation. A sharp edge nozzle tends to cause the onset of cavitation much closer to the inlet of the nozzle as compared to the ideal nozzle, even under supercharged conditions.

In high supercharging, a discharge coefficient derived specifically for sharp edge nozzles is applied to the Omega model to account for the sharp edge effect and other losses. In low supercharging, we propose a scaling parameter P_{sat}/P_i applied as shown in Eq. (13). Here G_{sat} is the mass flux assuming saturated initial conditions using Eq. (9), and G_{low} is the mass flux assuming low supercharging given by Eq. (12). The scaling P_{sat}/P_i maintains the saturated mass flux equation for saturated conditions where $P_i = P_{\text{sat}}$, and for low supercharging, biases the prediction towards that of the saturated equation. This is to account for the sharp edge effect increasing the tendency for cavitation, which is more prevalent in the predictions of the saturated mass flux equation.

$$G = \left(\frac{P_{\text{sat}}}{P_i}\right)G_{\text{sat}} + \left(1 - \frac{P_{\text{sat}}}{P_i}\right)G_{\text{low}} \tag{13}$$

The same scaling is also applied to the prediction of critical pressure given by Eq. (14). Equation (13) and (14) will be referred to as the "modified Omega model".

$$P_{\text{crit}} = \left(\frac{P_{\text{sat}}}{P_i}\right)P_{\text{crit,sat}} + \left(1 - \frac{P_{\text{sat}}}{P_i}\right)P_{\text{crit,low}} \tag{14}$$

The modified Omega model is only applicable in low supercharging, as determined by the η_{st} parameter described previously. For high supercharging cases, it is not applicable and the original Omega model for high supercharging, with an appropriate discharge coefficient, should be used.

H. Proposed Model

Due to the wide range of conditions and suitable equations, a hybrid model is proposed. This hybrid model is composed of 3 of the previously discussed models, and follows a multi-step process:
1) The Omega model's η_{st} parameter (Eq. 10) is used to determine if the initial state is in low or high supercharging.
2) If it is in high supercharging, the Omega model's high supercharging equation (Eq. 11) is used, and if in low supercharging, the modified Omega model (Eq. 13) is used, for the prediction of choking pressure and mass flow rate for all chamber pressures below the choking pressure.
3) For chamber pressures above the choking pressure, the Dyer model (Eq. 3) is used and connected to the choked regime using a blending function.

This combination of the Omega, the modified Omega, and the Dyer model is termed the "proposed model". The results of the proposed model are shown in Fig. 3.

I. Discussion of Discharge Coefficients

The SPI, HEM, Dyer, and Omega model require discharge coefficients to account for flow rate reduction due to frictional losses along the injector and inlet losses due to the geometry.

A liquid discharge coefficient is calculated based on semi-empirical equations involving the Reynolds (Re) number, length to diameter ratio, and sharp edge effects [1, 18].

The discharge coefficient is given by,

$$C_d = \frac{1}{\sqrt{4C_f \frac{L}{D} + K}} \tag{15}$$

Table 2 Specifications of cold flow data for axial injectors from the experimental campaign of Waxman [1]. The data is used for error calculation of analytical and numerical models.

Fluid Used	D (mm)	L/D	Range of Operating Pressures (MPa)
N_2O, CO_2	0.79	23.3	4.35 - 7.00
N_2O, CO_2	1.5	12	4.36 - 6.93
N_2O	1.93	9.5	4.40 - 6.91

where the skin-friction coefficient for smooth walls obtained from the Blasius solution [1] is given below,

$$C_f \approx 0.0791 Re_{\mathrm{D}}^{-1/4} \tag{16}$$

and K is the excess pressure drop constant. K is empirically determined and a representative value for sharp-edge inlets is given by Langhaar as 2.28 [18]. The C_{d} value varies slightly as the Re number changes, but is approximately 0.63 for all cases. This liquid discharge coefficient is applied to the SPI, HEM, and Dyer models.

For the Omega model, extensive studies of pressure relief valves, experimental validation and analytical calculations, suggest that for two-phase choked flow, the discharge coefficient should be determined assuming gas only flow, and for unchoked flow, the liquid discharge coefficient should be used [17]. Several common methods have been proposed to scale between these two discharge coefficients using the liquid volume fraction (among other parameters), with varying results [8, 17].

Empirical two-phase discharge coefficients based on cavitation number have been developed for critical CO_2 through similarly sized, sharp edge, straight orifices [19, 20]. The discharge coefficient is given by,

$$C_{\mathrm{d}} = 0.368 + 0.361\sqrt{K} \tag{17}$$

Where K is the cavitation number defined as,

$$K = \frac{P_{\mathrm{i}} - P_{\mathrm{sat}}}{P_{\mathrm{i}} - P_{\mathrm{o}}} \tag{18}$$

The empirical models, however, are based on two-phase inlet conditions instead of saturated liquid, and are only validated for cavitation numbers larger than unity.

However, for highly supercharged conditions, the cavitation number predicted by the Omega model at the critical pressure drop is exactly unity, due to the critical downstream pressure being exactly the saturation pressure. Hence the empirical model described above is applicable, and results in a choked discharge coefficient of about 0.73.

This value shows good agreement with data in the choked regions for injector elements in the range of length to diameter ratios of 10 to 25. In the unchoked regions the liquid discharge coefficient described previously is used.

For low supercharge levels, the discharge coefficient used with the high supercharged case above does not apply since the cavitation number is less than unity. The suitable discharge coefficient is in the range of 0.85, which is in agreement with the preliminary sizing suggestions for safety valves, and is close to the gas discharge coefficients used on many similarly sized orifices in valves. However, the use of a third discharge coefficient based on best practices is unnecessary since the section of the proposed model described in Eq. (13) caters to the effect and presents good results.

V. Results of Mass Flow Rate Models

A. Cold Flow Test Data

Waxman [1] conducted an extensive cold-flow test campaign utilizing supercharged N_2O and CO_2 for a variety of injector geometries across a range of inlet pressures. The data using straight port injectors with square edge entrance geometries was utilized in this paper to assess the performance of the analytical and CFD models. In total, 26 test cases were utilized, totalling over 2600 data points. Figure 2 shows the application of the mass flow models across a range of pressure drops for the upstream fluid conditions most comparable to the predicted engine depressurization. The aforementioned test conditions are detailed in table 2. and the predicted engine depressurization is seen in Fig. 8.

7
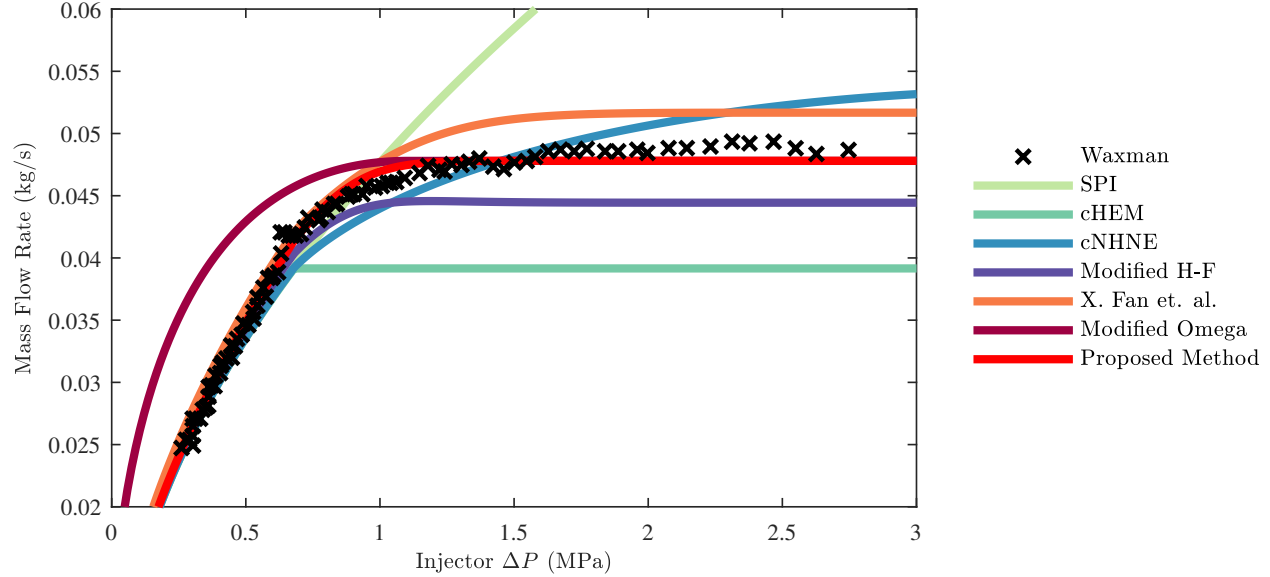
Fig. 2 Pressure drop and corresponding mass flow rate predictions of the models for a 1.5 mm, N$_2$O injector. Experimental data from identical Waxman [1] test case is also shown.

Table 3 Mass flow rate prediction error for the models adopted. For the critical models, the error is calculated for only the critical section. For all others it is calculated across the full range of pressure drops.

| Injector Diameter (mm)	Fluid	SPI (%)	cHEM (%)	cNHNE (%)	Modified Henry-Fauske (%)	X. Fan (%)	Modified Omega (%)	Proposed Model (%)
0.79	N$_2$O	7.22	6.79	6.50	3.20	26.10	2.01	6.71
0.79	CO$_2$	5.92	5.88	5.23	3.55	21.77	3.31	5.06
1.50	N$_2$O	4.44	3.68	2.73	5.82	14.46	4.24	2.69
1.50	CO$_2$	4.54	4.62	3.47	6.41	27.39	6.32	2.82
1.93	N$_2$O	3.25	1.22	1.64	4.80	26.81	10.01	1.97
MAPE		5.07	4.44	3.91	4.76	23.30	5.18	3.85

The mass flow model error is shown in table 3. It is evaluated through the mean absolute percentage error (MAPE) for every unique injector geometry and fluid combination across a range of upstream pressures and pressure drops. The MAPE is given by,

$$\text{MAPE} = \frac{1}{n} \sum_{i=1}^{n} \left| \frac{G_{\text{exp}_i} - G_{\text{model}_i}}{G_{\text{exp}_i}} \right| \tag{19}$$

B. Qualitative Mass Flow Model Evaluation

As seen in Fig. 2, for the relevant engine depressurization conditions, the SPI model reasonably predicts the flow rate for low pressure drops but it over-predicts without bound beyond the choking pressure as it does not account for critical flow. The HEM model under-predicts the flow rate for pressure drops larger than the critical pressure. The Dyer model shows agreeable results, however does not clearly indicate the critical mass flow rate since the SPI model it is partially based on does not choke. Both the X. Fan et. al. and modified Henry-Fauske model estimate the critical mass flow rate within a moderate margin. The proposed model can be seen to have the most accurate prediction of both the mass flow rate and the critical choking pressure. The proposed model and the experimental data are shown more clearly, unaccompanied, in Fig. 3.

8
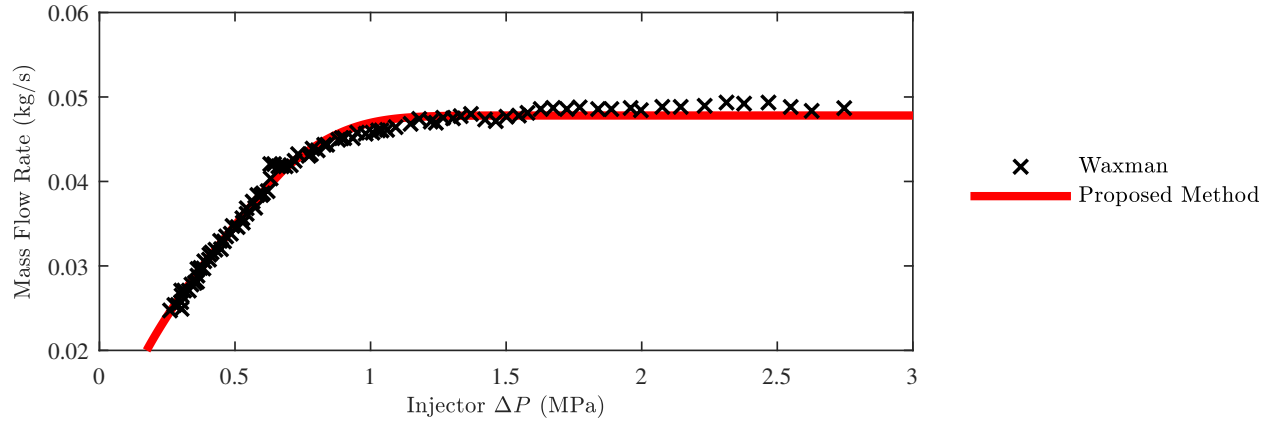
Fig. 3 **Pressure drop and corresponding mass flow rate prediction of the proposed model compared to experimental data from Waxman [1] test case with 1.5 mm diameter N_2O injector. Same test case is also used for CFD, the conditions for which are detailed in table 4.**

C. Global Error Study of Mass Flow Models

The critical HEM and SPI models that have been widely adopted in the field also have relatively low average errors due to the nature of the error function used. However they cannot reliably resolve the details required for the analysis such as the critical mass flow rate and pressure drop. The X. Fan et. al. model and the modified Henry-Fauske model have larger average errors. The X. Fan et. al. model specifically has the largest error due to being based on supercritical upstream conditions. Despite this it is still suitable for an initial design approach.

The Dyer model has an error less than 4%. The modified Omega model has a higher error. The distinction between them is in the source of the error. The Omega model has low error in the critical region, but high error in the unchoked region. The Dyer model is the inverse of this. From Fig. 2 the description above is clear, and it can be seen that the modified Omega model predicts the critical region well and the Dyer model predicts the unchoked region best. The proposed model combines these predictions and results in the lowest average error of less than 3.90%.

The proposed model has both the lowest numerical error (useful for depressurization predictions) and the best prediction of these critical parameters. Moreover, the proposed model has a mean error of less than 3% for injector elements in the range of length to diameter ratios of 12. Hence, it is suitable for use in hybrid rocket injector design in the current application.

Most importantly, the prediction of mass flow rate and critical choking pressure by the proposed model is accurate. Over the range of 26 test cases, the critical pressure is predicted to 6.13% of the experimental value by the proposed model. This is paramount in ensuring constant mass flow rate for the duration of the depressurization.

VI. CFD Simulation

In the previous sections of this paper a number of low-dimensional relations were presented and utilized for the purpose of design in order to quickly arrive at a prediction for two-phase mass flow rate through the injector. As was outlined, all the models had a sometimes narrow scope of usability and due to their low-dimensional and steady state nature, cannot be used to study flow over space or time.

The presence of cavitation inside an injector may alter the nominal velocity profile, turbulence level, spray and atomization characteristics [21]. This becomes problematic when modeling spray break-up and atomization processes as knowing the boundary conditions of the fluid at the exit plane of the injector element becomes crucial [22]. In order to solve for the fluid state at the exit plane of the injector, study the flow development along the injector channel as well as build confidence in the earlier analytical results, we turn to high fidelity CFD simulations.

A. Two-Phase Models Overview

Two-phase fluids are complex phenomenon that can manifest a wide range of properties. As such, the results of a two-phase fluid simulation may vary widely depending on the mathematical models chosen to represent the phenomena they exhibit. Therefore, the correct representation of a two-phase fluid is key to its solution [23, 24].

9
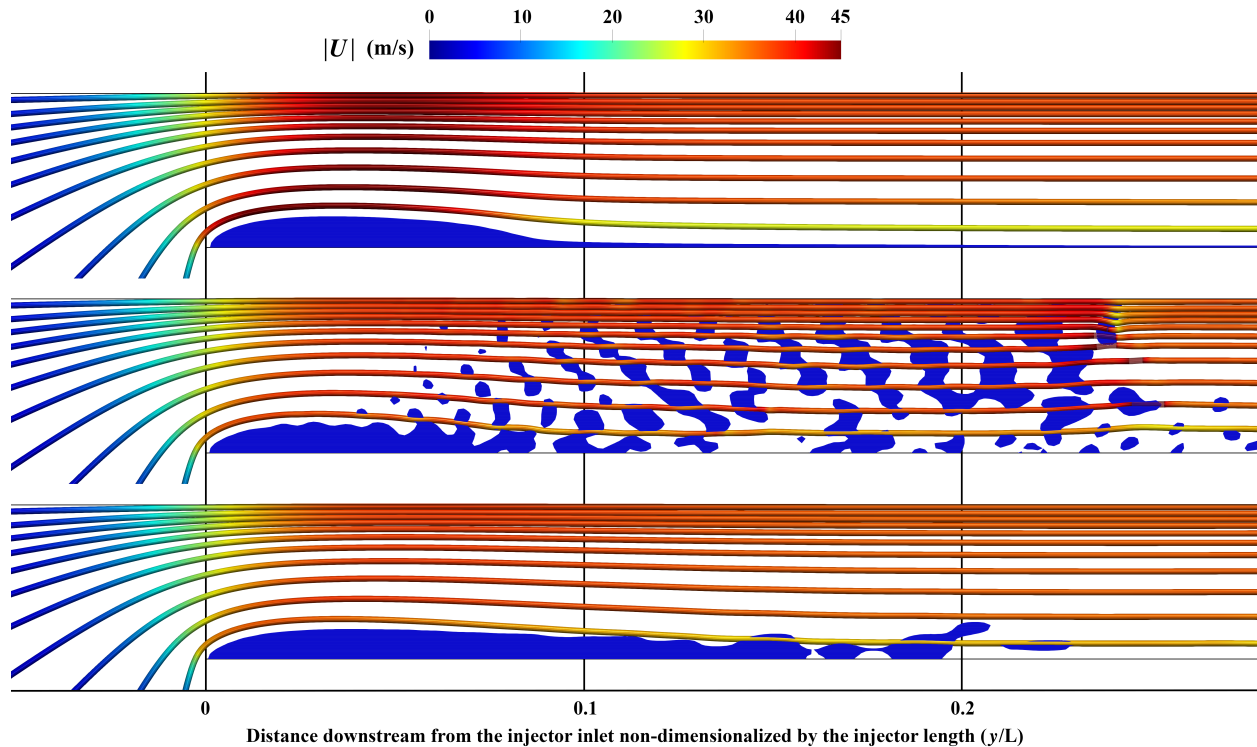
Fig. 4   Vapor cavity development for case I of table 4, as predicted by VOF (top), Euler-Euler (middle), and Euler-Euler-VOF (bottom) CFD methodologies. Streamlines coloured by velocity magnitude; Liquid volume fraction iso-volume for $\alpha = [0 \ 0.6]$ is shown in blue.

There have been a number of models developed in order to model two-phase fluids. Direct Numerical Simulation (DNS), where the Navier-Stokes equations are numerically solved without a turbulent closure model, remains the only model capable of accurately modeling the wide range of two-phase conditions that exist [25]. The lack of a turbulence model dictates the need to resolve all spatial and temporal scales of turbulence. In order to resolve the Kolmogrov microscales, which contain the smallest turbulent structures, a mesh on the order of $Re^{2.25}$ is required [26]. Cavitating flows in most cases are turbulent and therefore have a $Re > 2900$. Considering that an increase in Re by a factor of 2 leads to a 11 fold increase in computational cost [26], and the necessary minimum mesh size required, it is easy to see that DNS remains a purely academic solution. Other methods have been proposed, with RANS and LES turbulence closure most commonly, however they only work for particular cases due to their lack of generality [24].

Common methods for modeling multiphase flows include the one-fluid volume of fluid (VOF) approach, two-fluid Euler-Euler approach, as well as hybrid methods which combine different approaches. We will study the cavitation phenomena through an injector and the effect of these three CFD methodologies on its representation. The open-source CFD platform OpenFOAM [27], will be used for the entirety of this study.

B. Volume of Fluid Method

The Volume of Fluid Method (VOF) method treats the cavitating flow as a single fluid mixture and belongs to a class of interface tracking models with the aim of keeping the interface separation sharp so as to allow the study of mass transfer and surface tension at the interface [22]. The VOF approach works well when the characteristic length of the interface is larger than the grid size [23]. If the interfaces become smaller than the mesh used to discretize them, the model is unable to track the interface and the result loses its physical interpretation. As such, this model is unable to efficiently capture bubble formation or breakup and thus, is unable to model injector spray characteristics without restrictively high computational cost. This phenomena can result in numerical instabilities as well as noise at the interface [28]. Increasing the mesh density as well as modifying the numerical scheme used can reduce this problem without needing to alter the interface tracking approach [23].

The VOF formulation used in this study makes the following assumptions. No slip is assumed between phases thus

10

a single momentum equation is solved for the mixture. Local thermodynamic equilibrium is assumed, thus no energy equation is solved. The conservation of momentum equation as well the liquid volume fraction transport equation for the model are given as follows [29],

$$\frac{\partial (\rho \boldsymbol{U})}{\partial t} + \nabla \cdot (\rho \boldsymbol{U} \otimes \boldsymbol{U}) = -\nabla p + \nabla \cdot \boldsymbol{\tau} + \rho \boldsymbol{g} + \boldsymbol{F}_\sigma \tag{20}$$

$$\frac{\partial \alpha}{\partial t} + \nabla \cdot (\alpha \boldsymbol{U}) + \nabla \cdot [\alpha(1 - \alpha)\boldsymbol{U}_c] = \frac{\dot{m}}{\rho_l} \tag{21}$$

where p is pressure, ρ is density, $\boldsymbol{U}$ is velocity and $\boldsymbol{g}$ is gravity. The stress tensor for viscous and turbulent stresses is given by $\boldsymbol{\tau}$ and the mass transfer per unit volume due to cavitation is given by $\dot{m}$. The liquid volume fraction α is defined such that $\alpha = 1$ corresponds to a liquid phase with no cavitation, and $\alpha = 0$ corresponds to a fully cavitated, gas phase. The velocity term in the equations above is the phase-averaged velocity of the mixture and is thus defined as $\boldsymbol{U} = \alpha \boldsymbol{U}_l + (1 - \alpha)\boldsymbol{U}_g$, where the subscripts l and g indicate the liquid and gas phase respectively. Fluid properties for the mixture, including viscosity and density, are defined the same way.

The last term of the momentum equation is surface tension force which generates an additional pressure gradient at the interface and is calculated via Brackbill's Continuum Surface Force (CSF) method as [30],

$$\boldsymbol{F}_\sigma = \sigma \kappa \nabla \alpha \tag{22}$$

where σ is the fluid surface tension coefficient and the interface curvature is calculated as,

$$\kappa = -\nabla \cdot \left(\frac{\nabla \alpha}{|\nabla \alpha|} \right) \tag{23}$$

In order to counter phase diffusion at the interface, the liquid volume fraction transport equation, Eq. 21, includes the Compressive Interface Capturing Scheme for Arbitrary Meshes (CICSAM) [31], an interface compression method used to compress the interface by steepening the gradient of the volume fraction field. For this purpose, an artificial compression velocity $\boldsymbol{U}_c$ is introduced and defined as,

$$\boldsymbol{U}_c = C_\alpha |\boldsymbol{U}| \frac{\nabla \alpha}{|\nabla \alpha|} \tag{24}$$

The compression magnitude can be relaxed or increased with C_α.

C. Euler-Euler Method

The VOF method has a number of shortcomings resulting from its interface tracking approach, chief among these is the inability to efficiently model small interfaces. For such cases, Euler-Euler methodologies are the preferred method as they are able to model discrete flows smaller than the mesh size [23]. In this approach two phases share a common pressure but distinct velocities [22]. As a consequence of this, the set of governing equations for the system must be solved for each phase.

In the Euler-Euler methodology two phases are both assumed continuous throughout the entirety of the domain with no explicit interface. As a result, the derivation of the associated characteristic equations of the system require temporal and spatial averaging to occur [21]. Closure relationships for the transfer of mass, momentum and energy are needed to replace information lost by the averaging procedure [21]. The closure relationships combined with the averaged equations result in the Euler-Euler approach being capable and widely used to model two-phase flows whose characteristic interface lengths are smaller than the mesh size [23]. The necessary closure models are often in the form of empirical correlations which require experimental data and are often unable to describe more than one flow regime [32]. Thus, the accuracy of the simulation is dependent on the accuracy of the experimental data.

In the present Euler-Euler formulation, local thermodynamic equilibrium is assumed and only interfacial momentum and mass transfer will be taken into account. Interfacial momentum transfer, accounts for the average of the forces acting on the interface and can include the effects of drag force, lift force, virtual mass force, turbulent dispersion force and wall lubrication force. In the present work only the drag force is modeled.

The conservation of momentum equation as well the liquid volume fraction transport equation for the model, for each phase k, are given as follows [32],

$$\frac{\partial (\alpha_k \rho_k \boldsymbol{U}_k)}{\partial t} + \nabla \cdot (\alpha_k \rho_k \boldsymbol{U}_k \otimes \boldsymbol{U}_k) = -\alpha_k \nabla p + \nabla \cdot (\alpha_k \boldsymbol{\tau}_k) + \alpha_k \rho_k \boldsymbol{g} + \boldsymbol{F}_{\text{D},k} \tag{25}$$

$$\frac{\partial \alpha_k}{\partial t} + \nabla \cdot (\alpha_k \boldsymbol{U}_k) = \frac{\dot{m}}{\rho_k} \tag{26}$$

The drag force $\boldsymbol{F}_\text{D}$ acts opposite the direction of movement and is modeled based on the force acting on a single, spherical bubble. A constant, average bubble size obtained from CO_2 experiments is assumed [33], a valid approximation given the fluid similarities. As drag is the only momentum transfer term, it is solely responsible for the magnitude of the slip velocity between the phases. Considering each phase as continuous and discrete in turn, as denoted by the subscripts c and d respectively, the drag force is modeled as,

$$\boldsymbol{F}_{\text{D},k} = \frac{3}{4} \rho_\text{c} \alpha_\text{c} \alpha_\text{d} C_\text{D} \frac{|\boldsymbol{U}_\text{d} - \boldsymbol{U}_\text{c}| (\boldsymbol{U}_\text{d} - \boldsymbol{U}_\text{c})}{d_\text{d}} \tag{27}$$

The drag coefficient used in this study is that of Schiller & Naumann [34] given as,

$$C_\text{D} = \begin{cases} \frac{24}{Re} \left(1 + 0.15 Re^{0.687}\right) & \text{if } Re \leq 1000 \\ 0.44 & \text{if } Re > 1000 \end{cases} \tag{28}$$

The drag coefficient is calculated by independently considering each phase as the dispersed phase and taking a volume fraction weighted average of the two results.

D. Euler-Euler-VOF

From the discussion of VOF and Euler-Euler models it becomes clear that both have advantages and disadvantages. Continuous flow regimes can benefit from the interface tracking that the VOF method provides, whereas discrete flow regimes benefit from the empirical closure relations of the Euler-Euler method. A number of coupled models exist which can actively switch between the Euler-Euler method and a VOF method based on some actively calculated value function [23, 35], however they are outside the scope of this study. OpenFOAM implements an attempt to obtain some of the benefits of both methods in the form of an Eulerian solver with numerical sharpening applied at the interface [32]. This is done by including the aforementioned CICSAM and CSF methods, for interface compression and surface tension modeling respectively, in the momentum equations of the Eulerian solver. The conservation of momentum equation as well the liquid volume fraction transport equation for the model, for each phase k, are given as follows [32],

$$\frac{\partial (\alpha_k \rho_k \boldsymbol{U}_k)}{\partial t} + \nabla \cdot (\alpha_k \rho_k \boldsymbol{U}_k \otimes \boldsymbol{U}_k) = -\alpha_k \nabla p + \nabla \cdot (\alpha_k \boldsymbol{\tau}_k) + \alpha_k \rho_k \boldsymbol{g} + \boldsymbol{F}_{\text{D},k} + \boldsymbol{F}_{\sigma,k} \tag{29}$$

$$\frac{\partial \alpha_k}{\partial t} + \nabla \cdot (\alpha_k \boldsymbol{U}_k) + \nabla \cdot [\alpha_k (1 - \alpha_k) \boldsymbol{U}_\text{c}] = \frac{\dot{m}}{\rho_k} \tag{30}$$

E. Cavitation Models

The bulk of cavitation models propose that the governing relation that drives the growth of cavitation is the pressure difference across the surface of cavitation bubbles present [22]. Popular models in the literature that use this assumption include the Full Cavitation Model, Schnerr and Sauer model, Zwart model, Merkle model, and Kunz model [22, 36, 37]. All these models employ empirical coefficients that need to be tuned as they affect the stability and accuracy of the simulation results [36]. Of the aforementioned models, all except the Merkle and Kunz models are based on a simplified form of the Rayleigh-Plesset bubble dynamics equation. We consider the Kunz model in this study because of the minimal use of required empirical coefficients, its fast convergence [22], and its performance superiority compared to more theoretically sophisticated models [37].

12

The Kunz cavitation model is composed of a mass transfer source $\dot{m}^+$ and sink term $\dot{m}^-$ where the sum of two terms is the mass transfer as a result of the cavitation phenomena $\dot{m} = \dot{m}^+ + \dot{m}^-$. The source and sink terms of the Kunz model are [38],

$$
\dot{m}^+ = \frac{C_{\text{prod}}\, \rho_g \alpha^2 (1 - \alpha)}{t_\infty}
$$
$$
\dot{m}^- = \frac{C_{\text{dest}}\, \rho_g \alpha \min[0,\, p - p_{\text{sat}}]}{\rho_l \dfrac{U_\infty^2}{2} t_\infty}
$$

(31)

The freestream velocity U_∞ was calculated at the inlet using a SPI model and the mean flow time scale $t_\infty = \mathrm{L}/U_\infty$, was calculated with the injector element length as the characteristic length L. C_{prod} and C_{dest} are two empirically determined coefficients driving the condensation and evaporation process and must be tuned in order to provide the most accurate solution to the problem being modeled. The optimization of these parameters is the main source of difficulty associated with these cavitation models [22].

F. Case Setup

For turbulence closure we use the 2003 reformulation of the k-ω SST model [39]. Turbulence intensity is assumed to be 5% and the turbulent length scale is specified as the diameter of the injector. The time step throughout the simulations was not constant, rather it was a function of the local courant number $Co = U\Delta t/\Delta x$. The Co number was fixed at 0.2, and the time step Δt was automatically calculated based on local cell size Δx and fluid velocity U in order to not exceed the defined Co number. For quasi-transient and transient problems the Co number is typically below 1 to ensure numerical stability as it represents the number of cells that a fluid particle will cross in a single time step.

An axisymmetric, 2° wedge shaped mesh made up of 43,065 elements was created and is seen in Fig. 5. The mesh is composed of 96% hexahedral elements and contains 4 refinement zones progressively closer to the injector orifice. The most refined parts of the mesh were inside the injector element and its immediate surroundings. The domain boundaries are sufficiently far from the injector inlet and outlet to prevent wall effects from interfering with the internal flow. The mesh element size inside the injector was calculated such that the near wall region was within a $y+$ value of 30 to 150 in order to effectively utilize wall functions so as not to fully resolve the viscous sub-layer near the wall region.

In order to better study the flow and its development, the initial velocity for the entire domain was set to 0, only upstream and downstream pressures were specified. This allowed the flow to be entirely pressure driven. The domain from the inlet to 3/4 the injector length was initialized with liquid N_2O, with the rest of the domain being initialized with gaseous N_2O as suggested by [40].
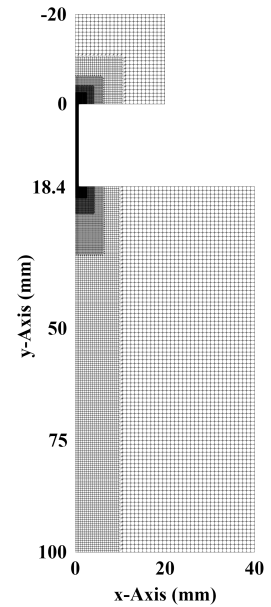

Fig. 5 Axisymmetric injector mesh.

VII. Overview and Results of CFD Simulations

In order to evaluate the three different CFD methodologies discussed in the previous section, simulations were run against four test cases from Waxman's experimental campaign for a 1.5 mm injector at the lowest value of N_2O supercharging. The points utilized are outlined in table 4. The specific points correspond to different levels of pressure drop ΔP across the injector and in order of increasing ΔP they represent the subcritical region, the critical inception point, and two sample pressure drops that occur during burn in the hybrid engine simulation seen in Fig. 8.

CFD mass flow rate predictions and their associated errors can be seen in Figs. 6 and 7 respectively. The development of the vapor cavity for Case I of table 4, as predicted by the different methodologies is seen in Fig. 4. Case I was chosen to be displayed as it has the lowest associated error magnitude for all methodologies and thus serves as a baseline comparison for the flow field. The predicted mass flow rate error is below 10% for nearly all simulations. Mass flow rate error is always lowest in the subcritical region with the lowest ΔP value and tends to increase with increasing ΔP. VOF results have the largest error magnitude followed by Euler-Euler, followed by Euler-Euler-VOF.

13
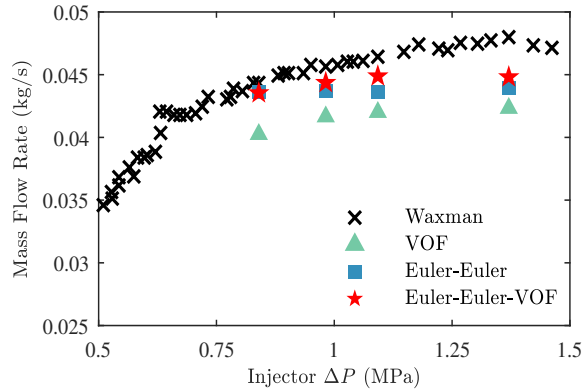
Fig. 6 Mass flow rate predictions of CFD simulations and experimental test case data.
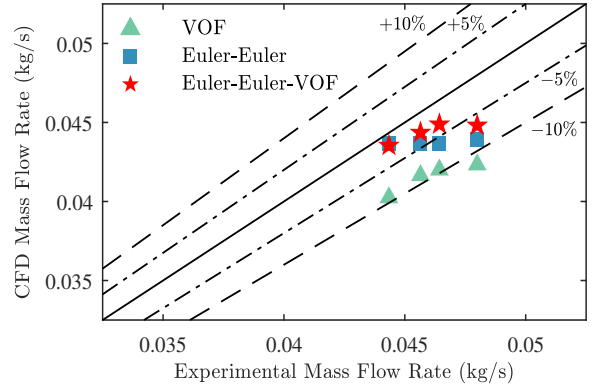
Fig. 7 Error associated with mass flow rate predictions of CFD simulations.

Table 4 Test conditions used in CFD simulations; Matched to points of interest in subset of Waxman [1] test case data and points in engine simulation.

Case	I	II	III	IV
State	Pre-Critical	Critical	Post-Critical	Post-Critical
ΔP (MPa)	0.84	0.98	1.09	1.37
P_i (MPa)	4.36	4.36	4.36	4.36
$P_{i, super}$ (MPa)	0.62	0.62	0.62	0.62
Fluid	N_2O	N_2O	N_2O	N_2O
D (mm)	1.5	1.5	1.5	1.5
L/D	12.3	12.3	12.3	12.3
T_i (K)	280	280	280	280

Although mass flow rate predictions of each methodology are reasonably close to one another, the associated flow fields vary greatly. The different flow field representations are a result of terms that each solver does or does not account for. The key differences between the formulations lie in the number of momentum equations solved, interface compression, surface tension force, and drag force.

At turbulent conditions of $Re > 5000$ a real world vena contracta becomes hydrodynamically unstable because of pressure gradients in its structure leading to the repeating, cavitation shedding behavior found in cavitating orifices [41]. This process is characterized by the growth of the inlet cavity, followed by the breakup and shedding of an attached vapor cloud portion which collapses as it is convected towards the injector outlet [41]. These cavitation dynamics are often classified through the non-dimensional Weber number defined as $We = \rho_g U_{rel}^2 d_p / \sigma$, whereas a larger Weber number predicts more aggressive forms of cavitation with higher tendencies for breakup and shedding to occur [42]. We can see that the Weber number is proportional to the velocity slip magnitude U_{rel}, which tends to disrupt the interface, and inversely proportional to the surface tension σ which tends to stabilize the interface [41].

As the VOF model solves only a single momentum equation to obtain common pressure and velocity, there is no relative velocity (slip) between the phases. Additionally, it models surface tension at the interface. Combined, this leads to a proportionally low We number, thus leading the VOF model to predict the stable gas sheet seen in Fig. 4.

The Euler-Euler model assumes two fluids sharing a common pressure and solves two momentum equations to obtain distinct velocities for each phase. The relative velocity arises from the inclusion of a drag model at the interface to account for interfacial momentum transfer. This model however does not take into account the restorative surface tension force, leading to a proportionally high We number. The effect of this approach is the immediate destabilization of the vena contracta after the injector inlet resulting in a high level of cloud breakup and shedding being predicted as seen in Fig. 4.

14
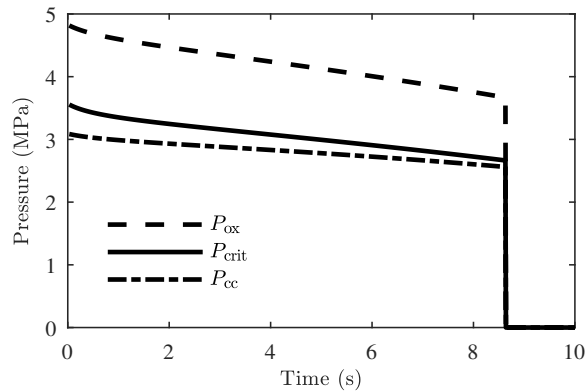
Fig. 8 Predicted pressures around injector from blow-down simulation. Critical pressure predicted by proposed model is also shown.
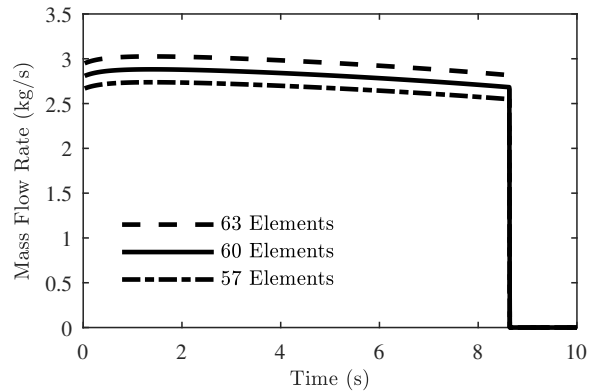
Fig. 9 Predicted mass flow rates of full injector used in engine simulation.

Lastly, the Euler-Euler-VOF model is the same as the Euler-Euler model but adds a surface tension and interface compression term, as present in the VOF model. Thus, of the models presented, it is the only model to take into account both the relative velocity as well as the surface tension. The combined effect of these two governing mechanisms results in a proportionally moderate We number, with moderate flow features that represent a combination of the VOF and Euler-Euler methodologies. As seen in Fig. 4, the vena contracta begins to experience instabilities as it extends down the length of the injector element, exacerbated by the slip magnitude between the phases and counteracted by the restoring surface tension. The instabilities grow downstream and eventually lead to vapor shedding being predicted which is convected down the element length.

The typical vapor shedding process found in cavitating orifices repeats in cycles which lead to mass flow rate oscillations [41, 43]. These oscillations can also be found in Waxman's mass flow rate data as seen in Fig. 2. The mass flow rate begins to oscillate as ΔP increases marking the start of the cavitation phenomenon. The oscillations grow in amplitude and wavelength as ΔP grows increasingly bigger marking the effect of progressively more extreme cavitation. This gives confidence in the vapor shedding prediction of the Euler-Euler-VOF methodology.

The formation of gas bubbles from the metastable phase causes a reduction in the local temperature due to the latent heat required to vaporize the fluid. This temperature fall reduces the saturation pressure, and leads to a delay in the growth of the cavitating bubbles termed "thermal delay" [4, 44]. The localized thermal effects tend to increase the mass flow rate, since the delay of bubble growth means the fluid remains in the liquid metastable phase for a longer time, and so has a higher average density. This increase in mass flow rate due to temperature drop is a distinct phenomenon separate from the boiling in the upstream tank. The boiling in the upstream tank causes a reduction in the local pressure, and hence a global decrease in mass flow rate as seen in the lower supercharging values of Waxman's test cases. When predicting the flow conditions using numerical simulations where the upstream pressure is maintained, accounting for the local thermal effects in the simulations may increase the predictions for mass flow rate and bring them closer to the experimental results. For all three CFD simulation methodologies, the mass flow rate is increasingly underpredicted as ΔP increases as seen in Fig. 6, it is theorized this is occurring as none of the methodologies are able to account for the local thermal delay which increases the mass flow rate through the injector.

VIII. Design Process

A process is presented for the design of hybrid rocket injectors. The aim of this process is to minimize the need for costly experimental validation by creating a design with as little error as possible prior to testing. CFD is ineffective for this purpose as it is slow compared to analytical models, however it can be used as an additional point of verification immediately preceding testing. The process is outlined in Fig. 10 and described in the following section.

The required input information for this process are the oxidizer and chamber pressures as a function of time (which may be determined using blow-down models), the desired mass flow rate (which arises from the combustion and thrust requirements) and a fixed injector length and total available area (which are geometric constraints from the structure of the rocket). The design variables are the quantity and diameter of the orifices and their arrangement.

15

Due to the X. Fan et. al. model's simplicity, and its dependence on length to diameter ratio, it can be used as a very quick calculation for the mass flow rate as a function of orifice diameter. In the present study, the process is validated for length to diameter ratios of 10 to 25, with the lowest error being for the ratio of 12. This is the basis of the chosen hole diameter, but other applications may have different requirements. The dependence of the length to diameter ratio in the X. Fan et. al. model is close to linear for the range of length to the diameter ratios considered, hence an optimum diameter must be chosen based on a preference for number of holes (possible symmetric arrangements), manufacturing constraints, total face area available, minimum hole spacing, or other constraining parameters.

With the diameter chosen, the critical pressure as a function of time can be determined by the proposed model. The ideal design would avoid chamber pressures below critical pressure and would maintain a sufficient margin of error in the difference of the chamber pressure and the critical pressure, so as to avoid unchoking the flow during the burn. The process here is detailed in Fig. 10 for improved clarity.

Performing the calculation above for the range of pressures over the burn, a prediction of the mass flow rate as a function of time is reached. Matching the time average mass flow rate calculated to the design mass flow rate gives a value of the number of holes required, that is more accurate than the initial value reached through the X. Fan et. al. empirical model. At this point the designer can return and adjust the diameter of the calculation if the number of holes is not satisfactory or does not fit the desired arrangement constraints. Once satisfied, the nominal injector arrangement is designed with the number of holes calculated, and two additional injectors are designed assuming under-prediction and over-prediction of the mass flow rate of an individual element by 5%. This yields an over-predicting injector with fewer holes than nominal and an under-predicting injector with more holes than the nominal case.

CFD can be performed at different operating conditions during depressurization and experimental validation of the 3 yielded designs can follow. This will quantify the errors and account for possible non-linearities in changing hole numbers. If the nominal design is not adequately close to the desired mass flow rate, the number of holes and arrangement can be modified, the new design retested, until the process converges onto a minimal error design.

IX. Example Design

The process described in the previous section was applied to the design of the Quasar engine. The duration of the burn is approximately 10 seconds, with a thrust of 6700 N. The oxidizer tank and chamber pressures are calculated using a blow-down [45] code and custom combustion simulation. For
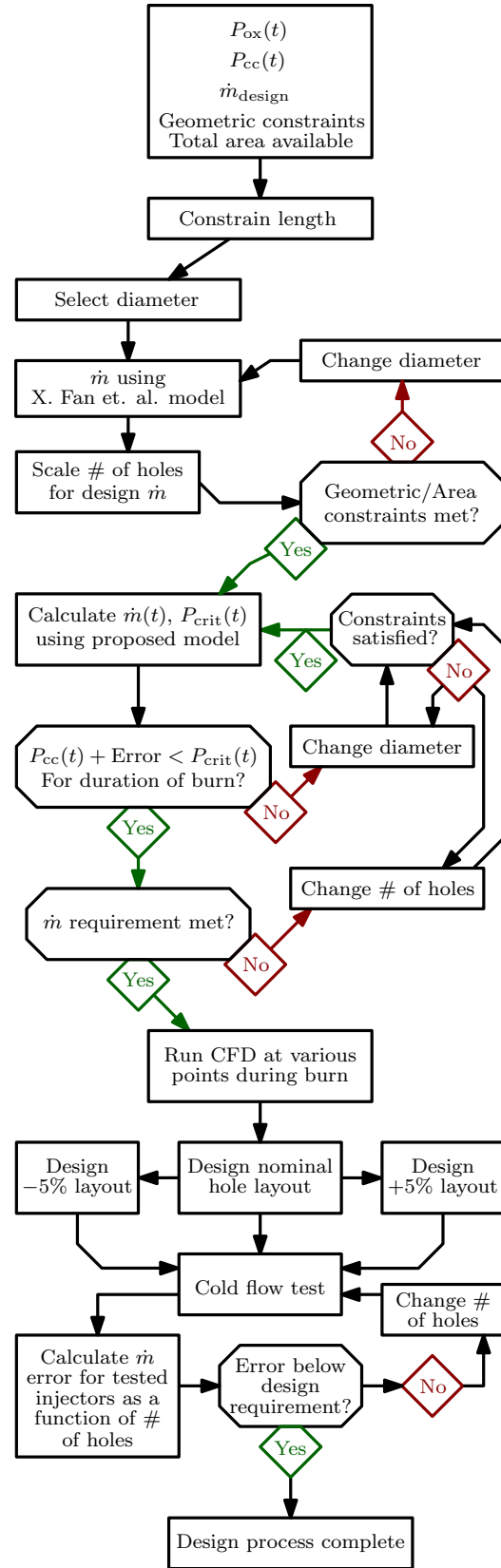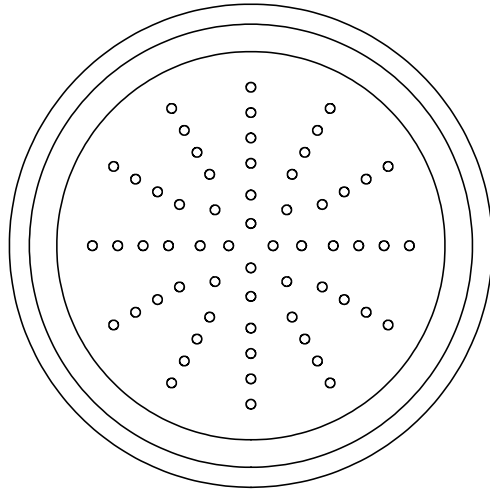

Fig. 10 Injector plate design process flow chart.

16

Fig. 11   Designed nominal injector.

the purpose of validating the analytical models in future cold flow experiments, the diameter and length were chosen as 1.5 mm and 18.4 mm, respectively, to allow reasonable comparison to Waxman's experimental data. The pressures during blow-down, as well as the predicted critical pressure by the proposed model, are shown in Fig. 8.

For an average design mass flow rate of 2.81 kg/s, the process resulted in a nominal 60 holes in the injector. Based on experiments by Gamper et. al. [2] on similar injectors with different layouts, it was shown that radially growing holes, arranged in the form of the solid fuel port (in this case circular) yielded the best performance with respect to combustion instability for hybrid rockets. The 60 hole nominal arrangement designed for the engine is shown in Fig. 11. The calculated mass flow rates for the 60 hole injector, as well as 63, and 57 hole arrangements (these are the under and over predicting cases, respectively), are shown in Fig. 9. Some notable results are outlined as follows. First, a slight initial increase in the mass flow rate due to increasing upstream pressure is observed. Second, despite the initial conditions being such that the difference between the chamber pressure and the predicted critical pressure is at least 12% (twice the 6% error on the critical pressure prediction), it reduces to 4% by the end of the burn, signalling that the flow may no longer be choked within the error bounds.

This highlights the utility of the proposed model in predicting the unchoking of the flow due to depressurization. With an increase of the oxidizer tank pressure by 200 kPa, the calculations provide a sufficient margin of error to ensure that the flow remains choked. This prediction may ensure reliable performance of the system and eliminate feed system coupled instabilities, leading to a safer and more reliable engine.

X. Conclusion

In this work a range of models and methods were adopted to design axial injectors for use in hybrid rockets. Due to the injector operating in a cavitating, two-phase flow regime, a combined model was proposed to better assess the performance of the injector. When compared with results of conventional models typically adopted in two-phase flow, the proposed model presented significant error reduction in the prediction of mass flow rate. The model was validated against experimental data from literature in the supercharged regime. The results show a 3.9% mass flow rate prediction error, making the proposed model a suitable choice for use in two-phase injector design. To validate the operation regime of the designed injector, a series of numerical simulations were performed using different solvers. The VOF, Euler-Euler, and Euler-Euler-VOF solvers captured a range of features such as cavity breakup and shedding. The simulations were verified against the available experimental data. The Euler-Euler-VOF model predicted the mass flow rate with the least error, 3.6%. An injector was designed for a N_2O-Paraffin hybrid rocket engine using the models and methods developed.

17

References

[1] Waxman, B. S., "An Investigation of Injectors for use with High Vapour Pressure Propellants with Applications to Hybrid Rockets," Ph.D. thesis, Stanford University, 2014.

[2] Gamper, E., and Hink, R., "Design and test of nitrous oxide injectors for a hybrid rocket engine," 2013. Deutscher Luft-und Raumfahrtkongress.

[3] Dabiri, S., and Sirignano, W. A., "Cavitation in an orifice flow," *Physics of Fluids*, Vol. 19, 2007. doi:10.1063/1.2750655.

[4] Brennen, C. E., "Cavitation and Bubble Dynamics," *Oxford University Press*, Vol. 44, 1995. doi:10.1017/CBO9781107338760, California Institute of Technology.

[5] Ebrahimi, B., He, G., Tang, Y., Franchek, M., Liu, D., Pickett, J., Springett, F., and Franklin, D., "Characterization of high-pressure cavitating flow through a thick orifice plate in a pipe of constant cross section," *International Journal of Thermal Sciences*, Vol. 114, 2017, pp. 229 – 240. doi:10.1016/j.ijthermalsci.2017.01.001.

[6] Tamaki, N., Shimizu, M., Nishida, K., and Hiroyasu, H., "Effects of Cavitation and Internal Flow on Atomization of a Liquid Jet," *Atomization and Sprays*, Vol. 8, 1998, pp. 179–197. doi:10.1615/AtomizSpr.v8.i2.30.

[7] Boccardi, G., Bubbico, R., Celata, G. P., and Mazzarotta, B., "Two-phase flowthrough pressure safety valves. Experimental investigation and model prediction," *Chemical Engineering Science*, Vol. 60, 2005, pp. 5284–5293. doi:10.1016/j.ces.2005.04.032.

[8] Leong, J. C., "A theory on the discharge coefficient for safety relief valve," *Journal of Loss Prevention in the Process Industries*, Vol. 17, 2004, pp. 301–313. doi:10.1016/j.jlp.2004.04.002.

[9] Yin, S., Weng, Y., Song, Z., Cheng, B., Gu, H., Wang, H., and Yao, J., "Mass transfer characteristics of pipeline leak-before-break in a nuclear power station," *Applied Thermal Engineering*, Vol. 142, 2018, pp. 194–202. doi:10.1016/j.applthermaleng.2018.06.077.

[10] Brown, S., Martynov, S., Mahgerefteh, H., and Proust, C., "A homogeneous relaxation flow model for the full bore rupture of dense phase CO2 pipelines," *International Journal of Greenhouse Gas Control*, Vol. 17, 2013, pp. 349 – 356. doi:10.1016/j.ijggc.2013.05.020.

[11] Lorenzo, D. M., Lafon, P., Seynhaeve, J.-M., and Y., B., "Benchmark of Delayed Equilibrium Model (DEM) and classic two-phase critical flow models against experimental data," *International Journal of Multiphase Flow*, Vol. 92, 2017, pp. 112–130. doi:10.1016/j.ijmultiphaseflow.2017.03.004.

[12] Dyer, J., Doran, E., Dunn, Z., Lohner, K., Zilliac, G., and Cantwell, B., "Modeling Feed System Flow Physics for Self-Pressurizing Propellants," *43rd AIAA/ASME/SAE/ASEE Joint Propulsion Conference*, 2007, pp. AIAA 2007–5702. doi:10.2514/6.2007-5702.

[13] Lemmon, E. W., Bell, I., Huber, M. L., and McLinden, M. O., "NIST Standard Reference Database 23: Reference Fluid Thermodynamic and Transport Properties-REFPROP, Version 10.0, National Institute of Standards and Technology," , 2018. doi:10.18434/T4JS3C.

[14] Bell, I. H., Wronski, J., Quoilin, S., and Lemort, V., "Pure and Pseudo-pure Fluid Thermophysical Property Evaluation and the Open-Source Thermophysical Property Library CoolProp," *Industrial & Engineering Chemistry Research*, Vol. 53, No. 6, 2014, pp. 2498–2508. doi:10.1021/ie4033999.

[15] Solomon, B. J., "Engineering Model to Calculate Mass Flow Rate of a Two-Phase Saturated Fluid Through An Injector Orifice," Master's thesis, Utah State University, 2011.

[16] Fan, X., Wang, Y., Zhou, Y., Chen, J., Huang, Y., and Wang, J., "Experimental study of supercritical CO2 leakage behavior from pressurized vessels," *Energy*, Vol. 150, 2018, pp. 342–350. doi:10.1016/j.energy.2018.02.147.

[17] Darby, R., "On two-phase frozen and flashing flows in safety relief values Recommended calculation method and the proper use of the discharge coefficient," *Journal of Loss Prevention in the Process Industries*, Vol. 17, 2004, pp. 255–259. doi:10.1016/j.jlp.2004.04.001.

[18] Langhaar, H., "Steady Flow in the Transition Length of a Straight Tube," *Journal of Applied Mechanics*, Vol. 64, 1942, pp. A55–A58.

[19] Tharakan, T. J., and Rafeeque, T., "The role of backpressure on discharge coefficient of sharp edged injection orifices," *Aerospace Science and Technology*, Vol. 49, 2016, pp. 269 – 275. doi:10.1016/j.ast.2015.12.014.

18

[20] Yu, B., Fu, P.-F., Zhang, T., and Zhou, H.-C., "The influence of back pressure on the flow discharge coefficients of plain orifice nozzle," *International Journal of Heat and Fluid Flow*, Vol. 44, 2013, pp. 509 – 514. doi:10.1016/j.ijheatfluidflow.2013.08.005.

[21] Gómez-Aldaraví, "Development of a computational model for a simultaneous simulation of internal flow and spray break-up of the Diesel injection process," Ph.D. thesis, Universitat Politècnica de València, 2014.

[22] Saha, Kaushik, "Modelling of cavitation in nozzles for diesel injection applications," Ph.D. thesis, University of Waterloo, 2014.

[23] Černe, G., Petelin, S., and Tiselj, I., "Coupling of the Interface Tracking and the Two-Fluid Models for the Simulation of Incompressible Two-Phase Flow," *Journal of Computational Physics*, Vol. 171, No. 2, 2001, pp. 776 – 804. doi: 10.1006/jcph.2001.6810.

[24] Damián, S. M., and Nigro, N. M., "The Detached Interphase Simulation," *Mecánica Computacional*, Vol. 32, 2013, pp. 1825–1847.

[25] Scardovelli, R., and Zaleski, S., "Direct Numerical Simulation of Free-surface and Interfacial Flow," *Annual Review of Fluid Mechanics*, Vol. 31, No. 1, 1999, pp. 567–603. doi:10.1146/annurev.fluid.31.1.567.

[26] Coleman, G. N., and Sandberg, R. D., "A primer on direct numerical simulation of turbulence – Methods, Procedures, and Guidlines," 2010. Aerodynamics and Flight Mechanics Research Group, University of Southampton, Technical Report AFM-09/01a.

[27] Weller, H. G., Tabor, G., Jasak, H., and Fureby, C., "A tensorial approach to computational continuum mechanics using object-oriented techniques," *Computers in Physics*, Vol. 12, No. 6, 1998, pp. 620–631. doi:10.1063/1.168744.

[28] Menon, S., "A Numerical Study Of Droplet Formation And Behavior Using Interface Tracking Methods," Ph.D. thesis, University of Massachusetts Amherst, 2011.

[29] Weller, H. G., "A New Approach to VOF-based Interface Capturing Methods for Incompressible and Compressible Flow," 2008. Technical Report.

[30] Brackbill, J., Kothe, D., and Zemach, C., "A continuum method for modeling surface tension," *Journal of Computational Physics*, Vol. 100, No. 2, 1992, pp. 335 – 354. doi:10.1016/0021-9991(92)90240-Y.

[31] Ubbink, O., and Issa, R., "A Method for Capturing Sharp Fluid Interfaces on Arbitrary Meshes," *Journal of Computational Physics*, Vol. 153, No. 1, 1999, pp. 26 – 50. doi:10.1006/jcph.1999.6276.

[32] Wardle, E. K., and Weller, G. H., "Hybrid Multiphase CFD Solver for Coupled Dispersed/Segregated Flows in Liquid-Liquid Extraction," *International Journal of Chemical Engineering*, Vol. 2013, 2013. doi:10.1155/2013/128936.

[33] Martínez, I., and Casas, P., "Simple model for CO2 Absorption in a bubbling water column," *Brazilian Journal of Chemical Engineering*, Vol. 29, 2012, pp. 107–111. doi:10.1590/S0104-66322012000100012.

[34] Schiller, L., and Naumann, A. Z., "Über die grundlegenden Berechnungen bei der Schwerkraftaufbereitung," *Vereines Deutscher Ingenieure*, Vol. 77, 1933, pp. 318–320.

[35] Yan, K., and Che, D., "A coupled model for simulation of the gas-liquid two-phase flow with complex flow patterns," *International Journal of Multiphase Flow*, Vol. 36, No. 4, 2010, pp. 333 – 348. doi:10.1016/j.ijmultiphaseflow.2009.11.007.

[36] Morgut, M., and Nobile, E., "Numerical Predictions of Cavitating Flow around Model Scale Propellers by CFD and Advanced Model Calibration," *International Journal of Rotating Machinery*, Vol. 2012, 2012, pp. 1–11. doi:10.1155/2012/618180.

[37] Hanimann, L., Mangani, L., Casartelli, E., and Widmer, M., "Steady-state cavitation modeling in an open source framework: Theory and applied cases," *6th International Symposium on Transport Phenomena and Dynamics of Rotating Machinery*, 2016.

[38] Kunz, R. F., Boger, D. A., Stinebring, D. R., Chyczewski, T. S., Lindau, J. W., Gibeling, H. J., Venkateswaran, S., and Govindan, T., "A preconditioned Navier-Stokes method for two-phase flows with application to cavitation prediction," *Computers & Fluids*, Vol. 29, No. 8, 2000, pp. 849 – 875. doi:10.1016/S0045-7930(99)00039-0.

[39] Menter, F. R., Kuntz, M., and Langtry, R., "Ten Years of Industrial Experience with the SST Turbulence Model," 2003, pp. pg. 625–632. In Proceedings of the fourth international symposium on turbulence, heat and mass transfer.

[40] Invigorito, M., Elia, G., and Panelli, M., "An Improved Approach for Hybrid Rocket Injection System Design," *International Journal of Aerospace and Mechanical Engineering*, Vol. 10, 2016.

[41] Ashgriz, N., *Handbook of Atomization and Sprays: Theory and Applications*, Springer US, 2011.

[42] Suh, H. K., Park, S. H., and Lee, C. S., "Experimental investigation of nozzle cavitating flow characteristics for diesel and biodiesel fuels," *International Journal of Automotive Technology*, Vol. 9, No. 2, 2008, pp. 217–224. doi:10.1007/s12239-008-0028-3.

[43] Wang, C., Huang, B., Wang, G., Zhang, M., and Ding, N., "Unsteady pressure fluctuation characteristics in the process of breakup and shedding of sheet/cloud cavitation," *International Journal of Heat and Mass Transfer*, Vol. 114, 2017, pp. 769 – 785. doi:10.1016/j.ijheatmasstransfer.2017.06.005.

[44] Zamansky, R., and Ham, F., "Modelization of cavitation in shear flows," *Center for Turbulence Research*, 2013. Stanford Annual Research Briefs.

[45] Fernandez, M. M., "Propellant tank pressurization modeling for a hybrid rocket," Master's thesis, Rochester Institute of Technology, 2009.